Computers and Fluids 154 (2017) 224–235

Contents lists available at ScienceDirect

Computers and Fluids

journal homepage: www.elsevier.com/locate/compfluid

Benchmark solutions

A high-order spectral method for nonlinear water waves in the presence of a linear shear current

Philippe Guyenne

Department of Mathematical Sciences, University of Delaware, DE 19716, USA

ARTICLE INFO

Article history:
Received 23 December 2016
Revised 23 May 2017
Accepted 8 June 2017
Available online 9 June 2017

Keywords:
Dirichlet–Neumann operator
Hilbert transform
Rogue waves
Pseudo-spectral method
Series expansion
Vorticity
Water waves

ABSTRACT

A direct numerical method is proposed to simulate nonlinear water waves with nonzero constant vorticity in a two-dimensional channel of finite or infinite depth. Such a vortical distribution represents a linearly varying shear current in the background flow. Our method is based on the reduction of this problem to a lower-dimensional Hamiltonian system involving surface variables alone. This is made possible by introducing the Dirichlet–Neumann operator and associated Hilbert transform which are described via a Taylor series expansion about the still water level. Each Taylor term is a sum of concatenations of Fourier multipliers with powers of the surface elevation, and thus is efficiently computed by a pseudo-spectral method using the fast Fourier transform. The performance of this numerical model is illustrated by examining the long-time evolution of Stokes waves on deep water and of solitary waves on shallow water. It is observed that a co-propagating current has a stabilizing effect on surface wave dynamics while a counter-propagating current promotes wave growth. In particular, the Benjamin–Feir instability of Stokes waves can be significantly reduced or enhanced. Our simulations also suggest the existence of stable rotational solitary waves if the vorticity is not too large in magnitude.

1. Introduction

The classical formulation for water waves assumes flow irrotationality and has been widely used in the literature. Under this assumption, the original Laplace problem can be reduced from one posed inside the fluid domain to one posed at the boundary alone. This is accomplished by using boundary integral operators and furthermore, in the absence of dissipative mechanisms, a canonical Hamiltonian formulation can be written in terms of surface variables alone [50]. The two conjugate variables are the surface elevation and the velocity potential evaluated at the free surface. This dimension reduction is quite advantageous for mathematical analysis and numerical simulation, and has contributed to the success of the irrotational formulation [47]. In particular, Craig and Sulem [17] showed that the dependence on the surface elevation can be made more explicit in the Hamiltonian functional by introducing the Dirichlet–Neumann operator, and they proposed an efficient and accurate numerical method for simulating nonlinear water waves based on a Taylor series expansion of this operator. On the analytical side, Zakharov's Hamiltonian formulation can also be used to obtain rigorous results on the nonlinear stability of solitary wave solutions.

In recent years, the free boundary problem for water waves with nonzero vorticity has drawn increasing attention from the mathematical community. This setting is of special relevance to problems in oceanography and coastal engineering where wave-current interactions may play a major role [40]. Much theoretical work has been done by Constantin, Strauss and coworkers to investigate the existence and properties (e.g. stability) of two-dimensional traveling wave solutions based on the stream function or Dubreil–Jacotin formulation of the Euler equations [10,24,32,48]. For constant vorticity, a Hamiltonian formulation similar to Zakharov's can be derived so that the governing equations can again be expressed in terms of surface variables involving the stream function and generalized velocity potential [9,45]. An alternative nonlocal formulation has been proposed by [2] via the use of integral equations. Recent progress has been made on extending these nonlocal equations to two-layer systems with constant (but distinct) vorticity in each fluid layer [8,19].

In addition to these theoretical results, numerical studies have also been conducted in the fully nonlinear two-dimensional setting. For example, Ko and Strauss [35] computed finite-depth periodic waves with general vorticity by solving the full equations in the Dubreil–Jacotin formulation. The moving fluid domain is mapped to a fixed rectangle where the bulk equations and boundary conditions are discretized by finite differences. Moreira and Peregrine [37] simulated nonlinear interactions between

E-mail address: guyenne@udel.edu

http://dx.doi.org/10.1016/j.compfluid.2017.06.004
0045-7930/

deep-water waves and variable currents via a boundary integral method where the rotational part of the underlying flow is specified by a distribution of singularities (point vortices). In earlier work, Vanden-Broeck [44] developed a similar method based on Cauchy's integral formula for constant vorticity. The latter case corresponds to a linear shear current and has also been examined by other investigators, including [20] who sought a numerical solution in the form of a perturbative series, [6] who used conformal mapping to derive a lower-dimensional system of equations more suitable for direct numerical simulation, and [23] who proposed an extension of the high-order spectral method of [21]. All the numerical studies mentioned above focused on wave solutions of Stokes type (i.e. periodic nonlinear wave trains). Recently, Castro and Lannes [5] extended Zakharov's Hamiltonian formulation to water waves with general vorticity but the resulting surface equations are coupled to a bulk equation for the vorticity, which requires a solution defined over the entire fluid domain. Based on this new formulation, Lannes and Marche [36] derived a convenient set of Green–Naghdi equations for rotational waves in the shallow-water regime, via the use of vertically averaged quantities, and investigated solitary wave solutions numerically.

In this paper, we extend the numerical approach of [17] to solving the full dynamical equations for two-dimensional nonlinear water waves with nonzero constant vorticity. This setting is of physical interest; e.g. tidal flows are well described by linear shear currents [42]. The starting point is the Hamiltonian formulation of [45] and [9], where such nonlocal operators as the Dirichlet–Neumann operator and associated Hilbert transform play a key role in the reduction to surface variables. The former operator gives the normal derivative of the velocity potential at the free surface, while the latter operator evaluates the stream function there. In light of their analyticity properties, both operators are expressed via a convergent Taylor series expansion about the unperturbed geometry of the fluid domain. Each term in these Taylor series is determined recursively as a sum of concatenations of Fourier multipliers with powers of the surface deformation, and thus is efficiently computed by a pseudo-spectral method using the fast Fourier transform. In doing so, we propose a new way of evaluating the Hilbert transform for Dirichlet data given on the boundary of an irregular domain. To our knowledge, this is the first time that the numerical approach of [17] is extended and applied to rotational water waves. A nice feature of this approach is that it can readily accommodate arbitrary water depth.

Our new contributions include: (i) a detailed derivation of the series expansion for the Hilbert transform as well as extensive convergence tests with respect to various physical and numerical parameters, (ii) the development of an efficient and accurate numerical model that directly solves the full time-dependent equations for nonlinear water waves with nonzero constant vorticity, and (iii) applications to nonlinear solutions in two distinct limiting regimes: Stokes waves on deep water and solitary waves on shallow water. In particular, we provide the first numerical evidence of stable rotational solitary waves from direct simulations of fully nonlinear and fully dispersive equations.

The remainder of this paper is organized as follows. Section 2 presents the mathematical formulation of the problem, including the basic governing equations and their surface reduction, as well as the Taylor series expansions for the Dirichlet–Neumann operator and associated Hilbert transform. Section 3 describes the numerical methods for spatial discretization and temporal integration of the reformulated equations. Section 4 shows numerical tests on the convergence of the Hilbert transform and applications of the numerical model to various types of wave solutions. The influence of vorticity on their dynamics is discussed and the conservation of invariants of motion is also assessed. Finally, concluding remarks are given in Section 5.

2. Mathematical formulation

2.1. Basic governing equations

We consider the motion of a free surface on top of a two-dimensional ideal fluid of uniform depth h. In Cartesian coordinates, the x-axis is the direction of wave propagation and the y-axis points upward. The free surface is assumed to be the graph of a function as given by $y = \eta(x,t)$. Denoting the velocity field by $\mathbf{u}(x,y,t) = \big(u(x,y,t), v(x,y,t)\big)^{\top}$, the equations of motion in the moving fluid domain

$$\Omega(t) = \{0 < x < L, -h < y < \eta(x,t)\},$$

are the Euler equations for mass conservation

$$u_x + v_y = 0, \tag{1}$$

and momentum conservation

$$u_t + uu_x + vu_y = -P_x, \qquad v_t + uv_x + vv_y = -P_y - g, \tag{2}$$

where $P(x, y, t)$ is the pressure (divided by the fluid density) and g is the acceleration due to gravity. Subscripts are shorthand notation for partial or variational derivatives (e.g. $u_t = \partial_t u$).

In the absence of surface tension, the boundary conditions at the free surface $\{y = \eta(x,t)\}$ are the dynamic condition

$$P = P_0, \tag{3}$$

where P_0 denotes the constant atmospheric pressure, and the kinematic condition

$$v = \eta_t + u\eta_x. \tag{4}$$

The boundary condition at the bottom $\{y = -h\}$ is the no-flow condition

$$v = 0. \tag{5}$$

This system of equations is conservative in the sense that the total energy

$$H = \iint_{\Omega} \left[\frac{1}{2}\big(u^2 + v^2\big) + gy\right] \mathrm{d}x\mathrm{d}y, \tag{6}$$

is conserved over time. In two dimensions, the vorticity $\gamma = v_x - u_y$ is simply advected by the flow and so if it is initially constant everywhere, then it remains so. Flows with nonzero constant vorticity are thus of interest and we hereafter assume γ to be a constant.

From (1), there exist two conjugate harmonic functions such that

$$\varphi_x = \psi_y = u + \gamma y, \qquad \varphi_y = -\psi_x = v, \tag{7}$$

where $\varphi(x, y, t)$ denotes the generalized velocity potential, $\psi(x, y, t)$ may be viewed as a stream function and the constant vorticity γ represents a background shear current that varies linearly in the vertical direction. With these new variables, Eq. (2) take the form

$$\nabla\left[\varphi_t + \frac{1}{2}\big(\varphi_x^2 + \varphi_y^2\big) + \gamma\psi - \gamma y\varphi_x + P + gy\right] = \mathbf{0},$$

which implies that the expression between brackets is a function $C(t)$ of time alone throughout the fluid. Absorbing $C(t)$ into the definition of φ yields

$$\varphi_t + \frac{1}{2}\big(\varphi_x^2 + \varphi_y^2\big) + \gamma\psi - \gamma\eta\varphi_x + g\eta = 0,$$

at the free surface, with the pressure jump set to zero by virtue of (3). The initial boundary value problem (1)–(5) can then be restated as

$$\Delta\varphi = 0, \quad \text{in} \quad \Omega(t), \tag{8}$$

$$\eta_t - \varphi_y + \varphi_x\eta_x - \gamma\eta\eta_x = 0\,, \quad \text{on} \quad y = \eta(x,t)\,, \tag{9}$$

$$\varphi_t + \frac{1}{2}\left(\varphi_x^2 + \varphi_y^2\right) + \gamma\psi - \gamma\eta\varphi_x + g\eta = 0, \quad \text{on} \quad y = \eta(x,t), \tag{10}$$

$$\varphi_y = 0\,, \quad \text{on} \quad y = -h\,. \tag{11}$$

Expressing $\nabla\varphi$ and ψ in terms of Dirichlet data for φ on the free surface requires the introduction of nonlocal operators as discussed next.

2.2. Hamiltonian formulation

Following [17,45] and [9], the dimensionality of the Laplace problem (8)–(11) can be reduced by introducing the trace of the velocity potential on the free surface,

$$\xi(x,t) = \varphi(x,\eta(x,t),t)\,, \tag{12}$$

together with the Dirichlet–Neumann operator (DNO)

$$G(\eta)\xi = (-\eta_x, 1)^\top \cdot \nabla\varphi\big|_{y=\eta}\,, \tag{13}$$

which is the singular integral operator that takes Dirichlet data ξ on $y = \eta(x,t)$, solves the Laplace Eq. (8) subject to (11), and returns the corresponding Neumann data (i.e. the normal fluid velocity there). Via this surface reduction, Eqs. (9) and (10) can be formulated as a non-canonical Hamiltonian system

$$\begin{pmatrix}\eta_t\\ \xi_t\end{pmatrix} = \begin{pmatrix}0 & 1\\ -1 & \gamma\partial_x^{-1}\end{pmatrix}\begin{pmatrix}H_\eta\\ H_\xi\end{pmatrix}, \tag{14}$$

for the conjugate variables η and ξ, whose Hamiltonian

$$H = \frac{1}{2}\int_0^L \left[\xi G(\eta)\xi - \gamma\xi_x\eta^2 + \frac{1}{3}\gamma^2\eta^3 + g\eta^2\right]\mathrm{d}x\,, \tag{15}$$

corresponds to the total energy (6).

In particular, all the spatial and temporal derivatives of φ on the free surface can be explicitly written in terms of η and ξ (and their derivatives) together with $G(\eta)\xi$. For this purpose, we use a number of identities, namely

$$\xi_t = \varphi_t + \varphi_y\eta_t\big|_{y=\eta}\,, \qquad \xi_x = \varphi_x + \varphi_y\eta_x\big|_{y=\eta}\,, \tag{16}$$

by differentiating (12) and using the chain rule, as well as

$$G(\eta)\xi = \varphi_y - \varphi_x\eta_x\big|_{y=\eta}\,,$$

by virtue of (13). This implies

$$\varphi_x = \xi_x - \varphi_y\eta_x\big|_{y=\eta}\,, \tag{17}$$

and

$$\begin{aligned}\varphi_y &= G(\eta)\xi + \varphi_x\eta_x = G(\eta)\xi + (\xi_x - \varphi_y\eta_x)\eta_x\big|_{y=\eta}\,,\\ &= G(\eta)\xi + \xi_x\eta_x - \varphi_y\eta_x^2\big|_{y=\eta}\,,\end{aligned}$$

which yields

$$\varphi_y\big|_{y=\eta} = \frac{1}{1+\eta_x^2}\left[G(\eta)\xi + \xi_x\eta_x\right]. \tag{18}$$

Then, by substituting (18) back into (17) and (16), we obtain

$$\begin{aligned}\varphi_x\big|_{y=\eta} &= \xi_x - \frac{\eta_x}{1+\eta_x^2}\left[G(\eta)\xi + \xi_x\eta_x\right],\\ &= \frac{1}{1+\eta_x^2}\left[\xi_x - \eta_x G(\eta)\xi\right],\end{aligned} \tag{19}$$

and

$$\begin{aligned}\varphi_t &= \xi_t - \varphi_y\eta_t\big|_{y=\eta},\\ &= \xi_t - \frac{1}{1+\eta_x^2}\left[G(\eta)\xi + \xi_x\eta_x\right]\left[G(\eta)\xi + \gamma\eta\eta_x\right],\\ &= \xi_t - \frac{1}{1+\eta_x^2}\left[(G(\eta)\xi)^2 + \gamma\eta\eta_x G(\eta)\xi + \xi_x\eta_x G(\eta)\xi + \gamma\eta\xi_x\eta_x^2\right].\end{aligned}$$

For the latter equation, we also used the fact that

$$\eta_t = \varphi_y - \varphi_x\eta_x + \gamma\eta\eta_x\big|_{y=\eta} = G(\eta)\xi + \gamma\eta\eta_x\,,$$

according to the kinematic condition (9) and the definition (13) of the DNO. Moreover, adding up the squares of (18) and (19),

$$\varphi_y^2\big|_{y=\eta} = \frac{1}{(1+\eta_x^2)^2}\left[(G(\eta)\xi)^2 + 2\eta_x\xi_x G(\eta)\xi + \eta_x^2\xi_x^2\right],$$

$$\varphi_x^2\big|_{y=\eta} = \frac{1}{(1+\eta_x^2)^2}\left[\xi_x^2 - 2\eta_x\xi_x G(\eta)\xi + \eta_x^2(G(\eta)\xi)^2\right],$$

leads to

$$\begin{aligned}\varphi_x^2 + \varphi_y^2\big|_{y=\eta} &= \frac{1}{(1+\eta_x^2)^2}\left[(1+\eta_x^2)\xi_x^2 + (1+\eta_x^2)(G(\eta)\xi)^2\right],\\ &= \frac{1}{1+\eta_x^2}\left[\xi_x^2 + (G(\eta)\xi)^2\right].\end{aligned}$$

Inserting these expressions into (9) and (10) gives a closed system of two equations

$$\eta_t = G(\eta)\xi + \gamma\eta\eta_x\,, \tag{20}$$

$$\begin{aligned}\xi_t = -g\eta - \frac{1}{2(1+\eta_x^2)}&\left[\xi_x^2 - (G(\eta)\xi)^2 - 2\xi_x\eta_x G(\eta)\xi\right]\\ &+ \gamma\eta\xi_x - \gamma K(\eta)\xi\,,\end{aligned} \tag{21}$$

where the trace of the stream function on the free surface is the Hilbert transform (HT) of ξ associated with the moving fluid domain, i.e.

$$\psi(x,\eta(x,t),t) = K(\eta)\xi\,,$$

and is related to the DNO by $G(\eta)\xi = -\partial_x K(\eta)\xi$. As shown in [45], system (14) can be brought into canonical form by using the Darboux coordinates η and ζ, where

$$\zeta = \xi - \frac{1}{2}\gamma\partial_x^{-1}\eta\,,$$

but here we prefer to consider (14) because it is a direct extension of Craig and Sulem's formulation and thus can be simulated by a similar numerical method. Eqs. (20) and (21) reduce to the classical Hamiltonian equations for irrotational water waves if $\gamma = 0$. Surface tension could be easily incorporated into (21) but will not be examined in this paper.

Other invariants of motion for (14) include the volume

$$V = \int_0^L \eta\,\mathrm{d}x\,,$$

and impulse

$$I = \int_0^L \left(\eta\xi_x - \frac{1}{2}\gamma\eta^2\right)\mathrm{d}x\,.$$

2.3. Dirichlet–Neumann operator and Hilbert transform

Owing to its analyticity properties with respect to η [7], the DNO can be expressed in terms of a convergent Taylor series expansion

$$G(\eta) = \sum_{j=0}^{\infty} G_j(\eta)\,, \tag{22}$$

where each term G_j is homogeneous of degree j in η and can be determined recursively [16]. More specifically, for $j = 2r > 0$,

$$\begin{aligned} G_{2r}(\eta) = {} & \frac{1}{(2r)!} G_0 D^{2(r-1)} D \eta^{2r} D \\ & - \sum_{s=0}^{r-1} \frac{1}{(2(r-s))!} D^{2(r-s)} \eta^{2(r-s)} G_{2s}(\eta) \\ & - \sum_{s=0}^{r-1} \frac{1}{(2(r-s)-1)!} G_0 D^{2(r-s-1)} \eta^{2(r-s)-1} G_{2s+1}(\eta)\,, \end{aligned}$$

and, for $j = 2r-1 > 0$,

$$\begin{aligned} G_{2r-1}(\eta) = {} & \frac{1}{(2r-1)!} D^{2(r-1)} D \eta^{2r-1} D \\ & - \sum_{s=0}^{r-1} \frac{1}{(2(r-s)-1)!} G_0 D^{2(r-s-1)} \eta^{2(r-s)-1} G_{2s}(\eta) \\ & - \sum_{s=0}^{r-2} \frac{1}{(2(r-s-1))!} D^{2(r-s-1)} \eta^{2(r-s-1)} G_{2s+1}(\eta)\,, \end{aligned}$$

where $D = -\mathrm{i}\partial_x$ and $G_0 = D\tanh(hD)$ are Fourier multiplier operators. In the infinite-depth limit ($h \to \infty$), G_0 reduces to $|D|$. Accordingly, the HT can also be expanded as a power series

$$K(\eta) = \sum_{j=0}^{\infty} K_j(\eta)\,, \tag{23}$$

where, for $j = 2r > 0$,

$$\begin{aligned} K_{2r}(\eta) = {} & -\frac{1}{(2r)!} K_0 D^{2(r-1)} \partial_x \eta^{2r} \partial_x \\ & - \sum_{s=0}^{r-1} \frac{1}{(2(r-s))!} D^{2(r-s-1)} \partial_x \eta^{2(r-s)} G_{2s}(\eta) \\ & - \sum_{s=0}^{r-1} \frac{1}{(2(r-s)-1)!} K_0 D^{2(r-s-1)} \eta^{2(r-s)-1} G_{2s+1}(\eta)\,, \end{aligned} \tag{24}$$

and, for $j = 2r-1 > 0$,

$$\begin{aligned} K_{2r-1}(\eta) = {} & \frac{1}{(2r-1)!} D^{2(r-1)} \eta^{2r-1} \partial_x \\ & - \sum_{s=0}^{r-1} \frac{1}{(2(r-s)-1)!} K_0 D^{2(r-s-1)} \eta^{2(r-s)-1} G_{2s}(\eta) \\ & - \sum_{s=0}^{r-2} \frac{1}{(2(r-s-1))!} D^{2(r-s-2)} \partial_x \eta^{2(r-s-1)} G_{2s+1}(\eta), \end{aligned} \tag{25}$$

by virtue of the relation $K(\eta)\xi = -\partial_x^{-1} G(\eta)\xi$, where $K_0 = \mathrm{i}\tanh(hD)$ is the HT for a uniform strip of thickness h. In the infinite-depth limit, K_0 reduces to $\mathrm{i}\,\mathrm{sgn}(D)$ but (24) and (25) remain unchanged. The HT of ξ is defined up to an additive constant in (21) but again this constant may be absorbed into ξ_t by simply redefining ξ.

Recursion formulas (24) and (25) can be closed to allow the various K_j's to be re-used as vector operations on ξ, yielding

$$\begin{aligned} K_{2r}(\eta) = {} & -\frac{1}{(2r)!} K_0 D^{2(r-1)} \partial_x \eta^{2r} \partial_x \\ & + \sum_{s=0}^{r-1} \frac{1}{(2(r-s))!} D^{2(r-s-1)} \partial_x \eta^{2(r-s)} \partial_x K_{2s}(\eta) \\ & + \sum_{s=0}^{r-1} \frac{1}{(2(r-s)-1)!} K_0 D^{2(r-s-1)} \eta^{2(r-s)-1} \partial_x K_{2s+1}(\eta), \end{aligned} \tag{26}$$

for $j = 2r > 0$, and

$$\begin{aligned} K_{2r-1}(\eta) = {} & \frac{1}{(2r-1)!} D^{2(r-1)} \eta^{2r-1} \partial_x \\ & + \sum_{s=0}^{r-1} \frac{1}{(2(r-s)-1)!} K_0 D^{2(r-s-1)} \eta^{2(r-s)-1} \partial_x K_{2s}(\eta) \\ & + \sum_{s=0}^{r-2} \frac{1}{(2(r-s-1))!} D^{2(r-s-2)} \partial_x \eta^{2(r-s-1)} \partial_x K_{2s+1}(\eta), \end{aligned} \tag{27}$$

for $j = 2r-1 > 0$. As a result, the G_j's no longer appear explicitly in (26) and (27). We point out that Wahlén [46] also used a series expansion for K but the corresponding K_j's were not determined explicitly from a closed and separate recursion formula. Moreover, the focus of this previous study was on asymptotics and thus it did not produce any numerical result.

These series expansions of the DNO and HT play a central role in our numerical approach as discussed in the next section. They require however that η be a single-valued graph of x and thus overturning waves, with a multivalued profile, are not permitted [26]. Such a formulation has been successfully used in other contexts, e.g. in perturbation calculations for surface gravity waves in single- and double-layer fluids [12–15,25,27,46], as well as in direct numerical simulations with uniform or variable water depth [11,17,28,30,49].

3. Numerical methods

3.1. Space discretization

For space discretization, we assume periodic boundary conditions in x (with $0 \le x \le L$) and use a pseudo-spectral method based on the fast Fourier transform (FFT). This is a particularly suitable choice for computing the DNO since each term in its Taylor series (22) consists of concatenations of Fourier multipliers with powers of η.

More specifically, both functions η and ξ are expanded in truncated Fourier series

$$\begin{pmatrix} \eta \\ \xi \end{pmatrix} = \sum_k \begin{pmatrix} \widehat{\eta}_k \\ \widehat{\xi}_k \end{pmatrix} e^{\mathrm{i}kx}.$$

Spatial derivatives and Fourier multipliers are evaluated in the Fourier space, while nonlinear products are calculated in the physical space on a regular grid of N collocation points. For example, if we wish to apply the zeroth-order operator G_0 to a function ξ in the physical space, we transform ξ to the Fourier space, apply the diagonal operator $k\tanh(hk)$ to the Fourier coefficients $\widehat{\xi}_k$, and then transform back to the physical space.

In practice, the Taylor series of the DNO and HT are also truncated to a finite number of terms,

$$G(\eta) \approx G^M(\eta) = \sum_{j=0}^{M} G_j(\eta)\,, \qquad K(\eta) \approx K^M(\eta) = \sum_{j=0}^{M} K_j(\eta)\,, \tag{28}$$

but thanks to analyticity properties of the DNO, a small number of terms (typically $M < 10 \ll N$) are sufficient to achieve highly accurate results [38]. The convergence of (28) will be further examined

in Section 4.1. Given the direct relation between G and K, it is natural to use the same truncation order M in both series. The computational cost for evaluating (28) is estimated to be $O(M^2 N \log N)$ via the FFT. Aliasing errors are removed by zero-padding in the Fourier space [4].

There are alternate ways of determining the DNO and HT. We may first evaluate (23) together with (26) and (27) for K and then simply compute G via $G = -\partial_x K$. Conversely, we might apply the inverse operator $-\partial_x^{-1}$ to G after calculating it from (22). While there is a singularity (or at least some indetermination) for $k = 0$ since ∂_x^{-1} corresponds to $(\mathrm{i}k)^{-1}$ in the pseudo-spectral framework, this difficulty could be overcome by "manually" setting the zeroth Fourier coefficient of $K(\eta)\xi$ to zero, because the HT is defined up to an additive constant which may be omitted as mentioned earlier. From a general perspective, both series expansions (22) and (23) are of interest in their own right. In particular, evaluating the HT via the closed formulas (26) and (27) is straightforward and avoids any issue at $k = 0$. This provides a new recursive procedure for efficiently computing the HT in boundary value problems with an irregular domain, independently of the DNO [34].

3.2. Time integration

Time integration of (20) and (21) is performed in the Fourier space so that the linear terms can be solved exactly by the integrating factor technique [17]. For this purpose, we separate the linear and nonlinear parts in (20) and (21). Setting $\mathbf{v} = (\eta, \xi)^\top$, these equations can be expressed as

$$\partial_t \mathbf{v} = \mathcal{L}\mathbf{v} + \mathcal{N}(\mathbf{v}) , \tag{29}$$

where the linear part $\mathcal{L}\mathbf{v}$ is defined by

$$\mathcal{L}\mathbf{v} = \begin{pmatrix} 0 & G_0 \\ -g & 0 \end{pmatrix} \begin{pmatrix} \eta \\ \xi \end{pmatrix} ,$$

and the nonlinear part $\mathcal{N}(\mathbf{v})$ is given by

$$\mathcal{N}(\mathbf{v}) = \begin{pmatrix} \big[G(\eta) - G_0\big]\xi \\ -\frac{1}{2(1+\eta_x^2)}\Big[\xi_x^2 - (G(\eta)\xi)^2 - 2\xi_x\eta_x G(\eta)\xi\Big] \\ \qquad + \gamma\eta\xi_x - \gamma K(\eta)\xi \end{pmatrix} .$$

Via the change of variables

$$\widehat{\mathbf{v}}_k(t) = \Theta(t)\widehat{\mathbf{w}}_k(t) ,$$

in the Fourier space, involving

$$\Theta(t) = \begin{pmatrix} \cos\big(t\sqrt{gG_0}\big) & \sqrt{\frac{G_0}{g}}\sin\big(t\sqrt{gG_0}\big) \\ -\sqrt{\frac{g}{G_0}}\sin\big(t\sqrt{gG_0}\big) & \cos\big(t\sqrt{gG_0}\big) \end{pmatrix} ,$$

system (29) takes the form

$$\partial_t \widehat{\mathbf{w}}_k = \Theta(t)^{-1}\widehat{\mathcal{N}}_k\big[\Theta(t)\widehat{\mathbf{w}}_k\big] ,$$

which only contains nonlinear terms and is solved numerically in time using the fourth-order Runge–Kutta scheme with constant step Δt. By converting back to $\widehat{\mathbf{v}}_k$, this scheme reads

$$\widehat{\mathbf{v}}_k^{n+1} = \Theta(\Delta t)\widehat{\mathbf{v}}_k^n + \frac{\Delta t}{6}\Theta(\Delta t)\Big(f_1 + 2f_2 + 2f_3 + f_4\Big) , \tag{30}$$

where

$$f_1 = \widehat{\mathcal{N}}_k\big(\widehat{\mathbf{v}}_k^n\big) ,$$

$$f_2 = \Theta\Big(-\frac{\Delta t}{2}\Big)\widehat{\mathcal{N}}_k\Big[\Theta\Big(\frac{\Delta t}{2}\Big)\Big(\widehat{\mathbf{v}}_k^n + \frac{\Delta t}{2}f_1\Big)\Big] ,$$

$$f_3 = \Theta\Big(-\frac{\Delta t}{2}\Big)\widehat{\mathcal{N}}_k\Big[\Theta\Big(\frac{\Delta t}{2}\Big)\Big(\widehat{\mathbf{v}}_k^n + \frac{\Delta t}{2}f_2\Big)\Big] ,$$

$$f_4 = \Theta(-\Delta t)\widehat{\mathcal{N}}_k\Big[\Theta(\Delta t)\big(\widehat{\mathbf{v}}_k^n + \Delta t f_3\big)\Big] ,$$

for the solution at time $t_{n+1} = t_n + \Delta t$. By definition, the integrating factor $\Theta(t)$ is the fundamental matrix of the linear system $\partial_t \widehat{\mathbf{v}}_k = \mathcal{L}\widehat{\mathbf{v}}_k$. Here all its entries are real-valued and, in the limit $k \to 0$, they reduce to

$$\Theta(t) = \begin{pmatrix} 1 & 0 \\ -gt & 1 \end{pmatrix} .$$

To obtain (30), we used the fact that $\Theta(t)$ is a semigroup and satisfies

$$\Theta(a+b) = \Theta(a)\Theta(b) , \qquad \Theta(a)^{-1} = \Theta(-a) .$$

These identities can be easily checked by direct calculation. In our simulations, we typically selected a time step in the range $\Delta t = 0.001$–0.01 (with $M = 6$ and $N = 1024$) as a good compromise between accuracy, stability and computational cost. As a reference, this range of values for Δt is thousands/hundreds times smaller than the linear wave period $\tau = 2\pi/\omega \simeq 7$ for $\gamma = 0$, $h = 1$ and $k = 1$. Given the fourth-order accuracy of our time-integration scheme, these values of Δt are quite reasonable.

It should be pointed out that, unlike $G(\eta)\xi$, the zeroth-order (i.e. linear) contribution $\gamma K_0\xi$ was not extracted from $\gamma K(\eta)\xi$ to be included in the integrating factor for a number of reasons. First, it would lead to a fundamental matrix $\Theta(t)$ with complex-valued entries that are singular for $k = 0$. Second, because $\gamma K_0\xi$ is a diagonal linear term in the equation for ξ_t and because K_0 remains bounded as $k \to \infty$, so do the corresponding temporal frequencies. The stiffness associated with $\gamma K_0\xi$ is thus rather mild and we did not feel the need for applying a special treatment.

In cases of large-amplitude or highly deformed waves, we found it necessary to apply filtering in order to stabilize the numerical solution so that it can be computed over a sufficiently long time. Otherwise, spurious high-wavenumber instabilities tend to develop, eventually leading to the computation breakdown. This issue may be related to ill-conditioning of the DNO in its series form (see Section 4.1) and may also be promoted by the specific nonlinearity of the problem. As a remedy, we apply a hyperviscosity-type filter of the form

$$\exp\left(-36\left|\frac{k}{k_{\max}}\right|^{36}\right) ,$$

to the Fourier coefficients $\widehat{\eta}_k$ and $\widehat{\xi}_k$ at each time step, where $k_{\max}$ denotes the largest wavenumber of the resolved wave spectrum. Such a filter has been commonly employed in direct numerical simulations of nonlinear fluid flows by spectral methods [31], and its form ensures that only energy levels at high wavenumbers are significantly affected. Therefore, if a sufficiently fine resolution is specified, this filtering technique can help suppress spurious instabilities while preserving the overall solution. It has been successfully used in our previous computations of irrotational water waves [28,49].

4. Numerical results

In this section, we present several tests to assess the performance of our numerical model. We first check the convergence of the HT series as a function of physical and numerical parameters. We then apply our model to simulating rotational wave dynamics in two distinct limiting regimes: Stokes waves on deep water and solitary waves on shallow water. For such computations in the time domain, we examine the wave profile evolution as well as the conservation of invariants of motion. Because the present paper is focused on the development and testing of our numerical approach,

we only show illustrative examples and postpone a more in-depth study to a future publication.

We non-dimensionalize (20) and (21) by using the characteristic scales $\mathcal{L}$ and $\mathcal{T}$ as unit length and unit time respectively. In the deep-water regime, $\mathcal{L}=1/k_0$ and $\mathcal{T}=1/\sqrt{gk_0}$ so that $g\to 1$ and $\gamma\to\gamma/\sqrt{gk_0}$ (k_0 denotes a characteristic wavenumber). In the shallow-water regime, $\mathcal{L}=h_0$ and $\mathcal{T}=\sqrt{h_0/g}$ so that $g\to 1$, $h\to h/h_0$ and $\gamma\to\gamma\sqrt{h_0/g}$ (h_0 denotes a characteristic water depth). For convenience, in the following, we retain the original notation for all the variables and parameters but the reader should keep in mind that these now refer to dimensionless quantities.

4.1. Convergence of the HT

The DNO has been shown to be analytic in η provided the latter satisfies certain regularity conditions [7]. It follows that the DNO can be written in terms of a convergent Taylor series expansion and the convergence should be exponential with respect to the truncation order. This property has been investigated numerically by e.g. [38] and [49].

Naturally, we may wonder if this is also true for the series expansion (23) of the HT. Because the DNO and HT only differ by an application of $-\partial_x^{-1}$ (or vice versa $-\partial_x$), it is reasonable to assume that they have the same dependence on η and thus share the same analyticity property. The recursion formulas for the K_j's also share similarities with those for the G_j's, and so there may be numerical issues related to the convergence of the HT series. The convergence proof for DNOs by [38,39] should be directly applicable to the HT in this context.

Here we address these questions by considering a simple case where the numerical approximation (28) is compared with an exact expression of the HT. For this test, time is frozen and the domain (i.e. the free surface) is prescribed. By definition, the stream function and generalized velocity potential are conjugate harmonic functions, i.e. they both satisfy the Laplace Eq. (8) and are related by the Cauchy–Riemann Eq. (7). Accordingly, we can choose the monochromatic (single-mode) solutions

$$\psi=\sinh\big[k(y+h)\big]\cos(kx)\,,\qquad \varphi=\cosh\big[k(y+h)\big]\sin(kx)\,, \tag{31}$$

together with

$$\eta=a\cos(kx)\,, \tag{32}$$

for the surface profile. Note that the choice (31) also satisfies the no-flow condition (5) at the bottom. An exact expression of the HT can be obtained by inserting (32) into (31), yielding

$$K^E(\eta)\xi=\psi(x,\eta)=\sinh\big[k(\eta+h)\big]\cos(kx)\,.$$

The numerical approximation of the HT is computed via the truncated series (28) acting on

$$\xi=\varphi(x,\eta)=\cosh\big[k(\eta+h)\big]\sin(kx)\,,$$

as given by (31).

Fig. 1 shows the relative L^∞ error

$$\text{Error}=\frac{\|K^E(\eta)\xi-K^M(\eta)\xi\|_\infty}{\|K^E(\eta)\xi\|_\infty}\,,$$

between $K^E(\eta)\xi$ and $K^M(\eta)\xi$, as a function of M for various amplitudes a in cases of a slowly varying surface profile ($k=1$) and a rougher one ($k=10$). The computational domain is specified to be of length $L=2\pi$ and depth $h=1$, and is discretized with $N=1024$ grid points (corresponding to grid size $\Delta x=0.006$). A general observation is that the lower the amplitude a, the smaller this error and the faster the convergence. Smoothness of the surface profile

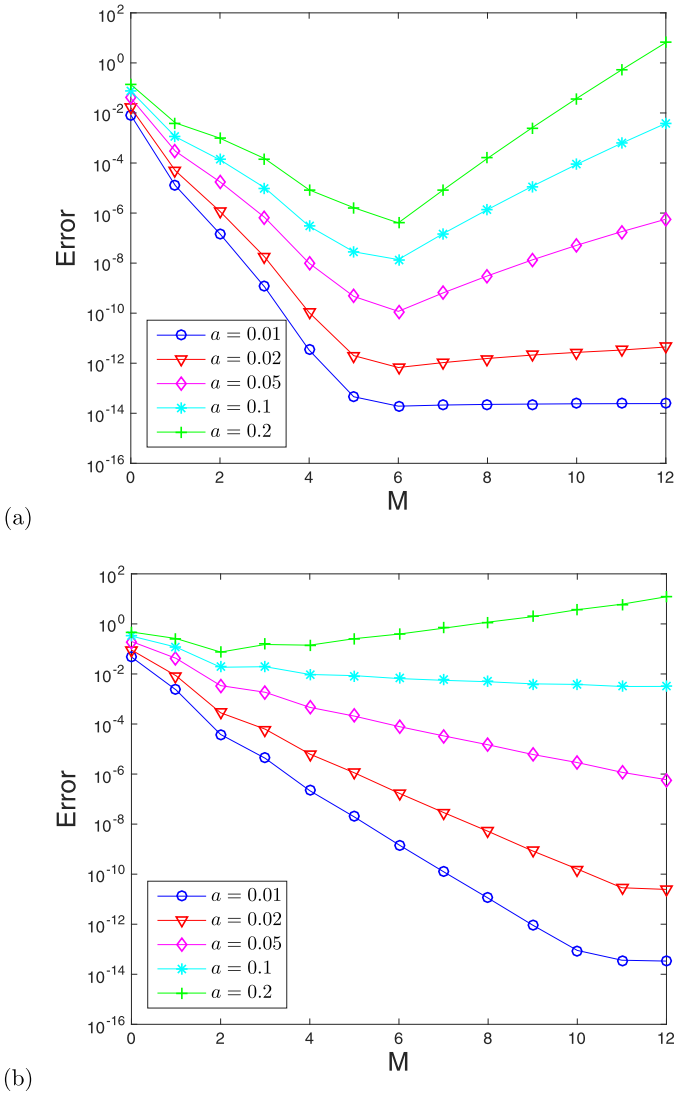

Fig. 1. Relative L^∞ error on the HT as a function of M for a sinusoidal surface profile η of varying amplitude a with wavenumber (a) $k=1$ and (b) $k=10$. The spatial resolution is $N=1024$.

also helps improve convergence. Exponential decay is well reproduced by the negative slopes in our semilog plots. For $k=1$ and $a=0.01$, the error quickly falls down to near machine precision and stagnates there past $M=6$. However, as a increases, the convergence is seen to dramatically deteriorate leading to a sharp error growth past $M=6$. This phenomenon is an illustration of the numerical ill-conditioning of operator expansion methods as previously reported in numerical studies involving the DNO [38,49]. Such methods rely heavily on cancellations of terms to ensure series boundedness but, in practice, terms are not canceled exactly due to round-off errors which are then amplified through the recursive process. This issue is less pronounced for $k=10$, possibly because the convergence is slower in this case. For such a rough surface, errors vary more monotonically with respect to M and, only if a is large enough (say $a=0.2$), some error growth is discernible past $M=2$. Note that the sudden loss of convergence as M increases is also observed when fixing a and k while varying N, as depicted in Fig. 2. The larger N, the smaller the critical value of M above which errors quickly grow. This is consistent with the fact that the number and order of Fourier multipliers in (26) and (27) increase with M, and their presence tends to amplify numerical errors most severely in the highest Fourier modes.

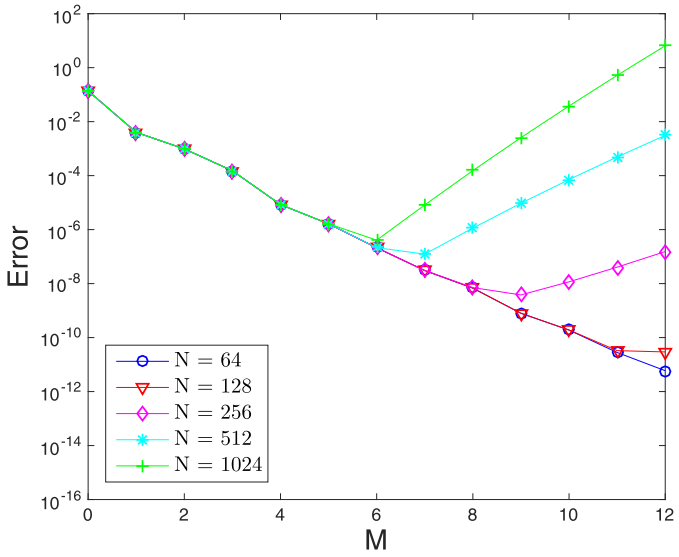

Fig. 2. Relative L^∞ error on the HT as a function of M for a sinusoidal surface profile η of amplitude $a = 0.2$ and wavenumber $k = 1$ with varying resolution N.

4.2. Stokes waves on deep water

We now turn our attention to the Benjamin–Feir instability (BFI) of Stokes waves in the presence of a linear shear current. For this purpose, we solve (20) and (21) with initial conditions of the form

$$\eta(x,0) = \Big[1 + A\cos(qx)\Big]\eta_0(x),$$
$$\xi(x,0) = \Big[1 + A\cos(qx)\Big]\xi_0(x), \tag{33}$$

where (η_0, ξ_0) denote a Stokes wave solution to (8)–(11) with $\gamma = 0$, which is computed by Fenton's method [22]. The Stokes wave is defined by its amplitude a and carrier wavenumber κ, and its steepness is given by $\varepsilon = \kappa a$. The parameters A and q in (33) represent the amplitude and wavenumber of the initial sideband perturbation. This is a physically relevant setting that may correspond to swell waves propagating into an oceanic area dominated by a strong background current. In the irrotational water wave problem, it is well known that Stokes waves are unstable to sideband perturbations on deep water [3]. It is thus of interest to investigate the effects of constant vorticity on Stokes wave evolution, in particular whether vorticity can enhance or prevent the BFI. Both signs of γ are considered here. We specify a spatial domain of length $L = 2\pi$ and infinite depth $h = \infty$, which is discretized with $N = 1024$ collocation points. The temporal resolution is given by $\Delta t = 0.001$ and the truncation order is set to $M = 6$ based on the previous convergence tests. This value of M should be more than enough to describe the BFI since this phenomenon is predominantly governed by four-wave resonant interactions (which correspond to $M = 2$).

We run simulations of (20) and (21) up to $t = 1000 \gg \tau$ starting from (33) with $(a, \kappa) = (0.005, 10)$ and $(A, q) = (0.1, 1)$ such that $\varepsilon = 0.05$. The sideband wavenumber $q = 1$ corresponds to the maximum of the growth rate

$$\sigma = \varepsilon^2\sqrt{g\kappa}\left(\frac{q}{2\sqrt{2}\kappa\varepsilon}\right)\sqrt{1 - \left(\frac{q}{2\sqrt{2}\kappa\varepsilon}\right)^2},$$

as predicted by a weakly nonlinear analysis based on the nonlinear Schrödinger (NLS) equation [3]. This initial disturbance serves to suitably trigger the BFI by promptly exciting the potentially most unstable mode. Nevertheless, for such a smooth perturbation of a moderately steep Stokes wave, this instability still takes a long time to develop. Figs. 3 and 4 show snapshots of η at the initial time $t = 0$ for $\gamma = 0$ and at the time of maximum growth (when the wave profile exhibits the highest crest) for various values of the vorticity ($\gamma = 0, \pm 0.5, \pm 1, \pm 2$). For the sake of comparison, we use the same initial condition in all these cases and only consider the time interval $0 \le t \le 1000$. The waves travel from left to right in the positive x-direction. Note that $\gamma > 0$ corresponds to primarily co-propagating currents (directed rightward) because it contributes positively to the horizontal fluid velocity $u = \varphi_x - \gamma y$ for $y < 0$, while $\gamma < 0$ represents primarily counter-propagating currents (directed leftward).

We see that a co-propagating current tends to stabilize the Stokes wave; the larger γ, the stronger the stabilizing effect. For $\gamma = +1$ and $\gamma = +2$, the BFI seems to be inhibited. The wave experiences a recurring sequence of small-amplitude modulations and demodulations about its initial configuration. As a result, the initial wave profile is overall preserved (modulo translation) up to at least $t = 1000$. The corresponding graphs are not shown here for convenience since they look almost identical to Fig. 3a. On the other hand, a counter-propagating current (moving in opposite direction to the Stokes wave) tends to promote and enhance its instability. The larger $|\gamma|$, the sooner the Stokes wave becomes unstable and the higher it grows. This wave amplification can be quite significant as indicated in Fig. 4. For $\gamma = -1$ and $\gamma = -2$, the wave reaches an elevation $a_{\max} = 0.016$ and $a_{\max} = 0.025$ at $t = 586$ and $t = 376$ respectively, which corresponds to a factor of $\alpha = 3.2$ and $\alpha = 5$ compared to the initial unperturbed wave amplitude $a = 0.005$. As a reference, the maximum wave growth observed in Fig. 3b for $\gamma = 0$ is $\alpha = 2.4$ ($a_{\max} = 0.012$), which agrees with the NLS prediction

$$\alpha = \frac{a_{\max}}{a} = 1 + 2\sqrt{1 - \left(\frac{q}{2\sqrt{2}\kappa\varepsilon}\right)^2} = 2.4,$$

for $\kappa = 10$, $\varepsilon = 0.05$ and $q = 1$. In the case $\gamma = -2$, the wave focusing at $t = 376$ is so strong that the computer code breaks down shortly afterward. These computations support the fact that wave-current interactions constitute a possible mechanism for rogue wave formation [33]. Similar numerical results were obtained by [6] and [23].

As an illustration, Fig. 5 plots the time evolution of errors

$$\text{Error} = \left|\frac{H - H_0}{H_0}\right|, \qquad \left|\frac{I - I_0}{I_0}\right|, \qquad |V - V_0|,$$

on energy H, impulse I and volume V respectively, for $\gamma = \pm 1$. The quantities H_0, I_0 and V_0 denote their initial values at $t = 0$. Note that, for V, we simply examine the absolute error rather than the relative error because V_0 is essentially zero for such a periodic wave train as the Stokes wave. The integrals in the definition of H, I and V are evaluated by the trapezoidal rule. We see that all three invariants of motion are very well conserved in our numerical simulations, with the errors on V remaining near machine precision. The errors on H and I are a few orders of magnitude higher than those for V, and they tend to coincide, probably because the computation of H and I involves several quantities including η and ξ_x while that for V only involves η. Another observation is that the errors for $\gamma = +1$ are a bit lower and their variation is smoother than those for $\gamma = -1$. This is consistent with previous observations from Fig. 3 and reflects the fact that "not much is going on" in the presence of a co-propagating current. As expected, for $\gamma = -1$, the errors on H and I exhibit more variation near $t = 586$ when the maximum wave growth occurs.

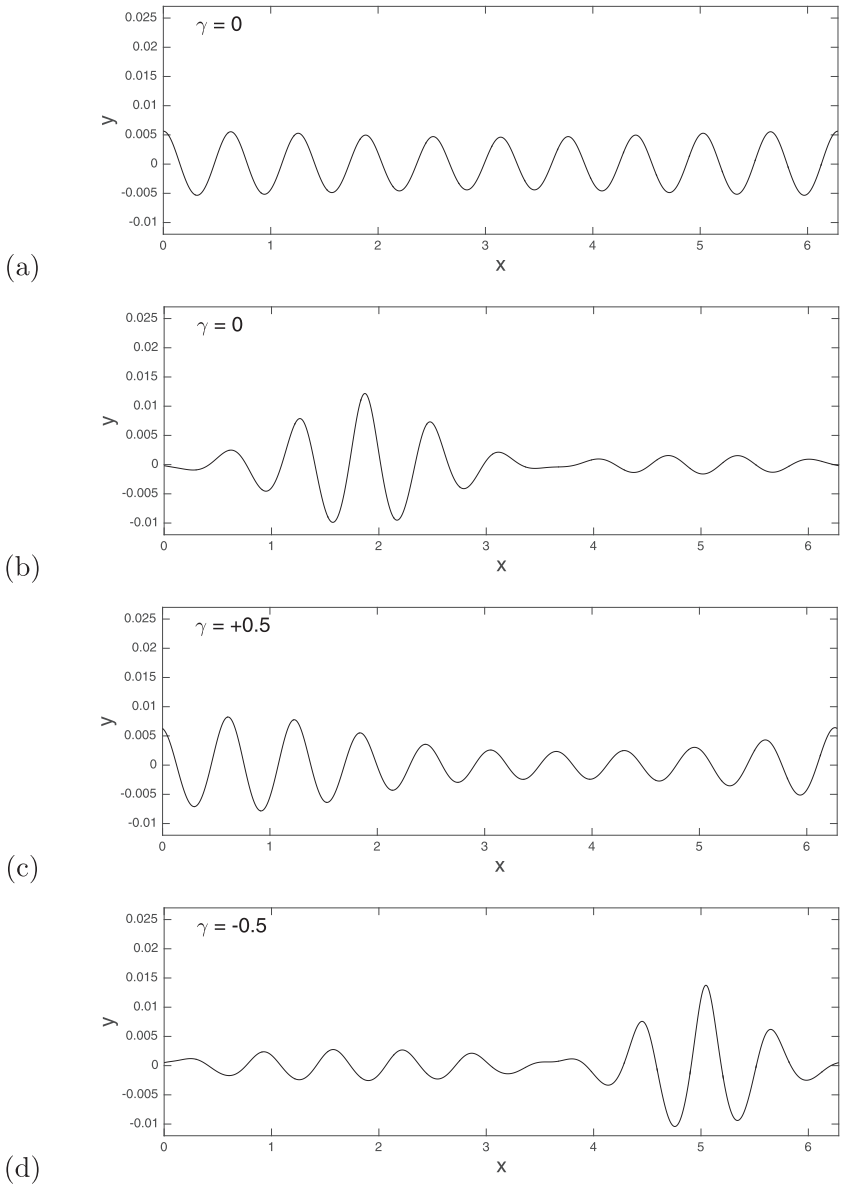

Fig. 3. Snapshots of η at (a) $t = 0$ ($\gamma = 0$), (b) $t = 956$ ($\gamma = 0$), (c) $t = 994$ ($\gamma = +0.5$) and (d) $t = 740$ ($\gamma = -0.5$) for an initially perturbed Stokes wave of amplitude $a = 0.005$ and wavenumber $\kappa = 10$ on deep water.

4.3. Solitary waves on shallow water

Finally, we consider the propagation of solitary waves on shallow water with constant vorticity. These long coherent waves are known to have strong stability properties in the irrotational case [11]. Therefore, we simply perform simulations with initial conditions given by a single solitary-wave solution of (8)–(11) for $\gamma = 0$, and examine their evolution as they travel through the rotational field. This initial condition is computed by Tanaka's method [43], and propagates steadily without change of shape and speed in the absence of vorticity. The domain length and depth are set to $L = 150$ and $h = 1$, with a spatial resolution of $N = 1024$ grid points (corresponding to $\Delta x = 0.146$). The spatial domain is specified long enough to accommodate the broad support of shallow-water solitary waves, hence a very fine grid size is not needed to accurately resolve their profile. Accordingly, the time step is chosen to be $\Delta t = 0.01$ but the truncation order is kept at $M = 6$ to ensure that we capture well the nonlinear character of such solutions. This value of M has been found to be suitable from our prior numerical work on solitary waves [11,29].

We run simulations of (20) and (21) up to $t = 500$ starting from an irrotational solitary wave of height $a = 0.3$ (relative to $h = 1$). Again, the same initial condition is used in all cases being considered and wave propagation is prescribed to go from left to right. Fig. 6 shows snapshots of η at various times for $\gamma = 0, \pm 0.5$. In the presence of a co-propagating current, the solitary wave is seen to gradually decrease in amplitude and broaden in width. However, an equilibrium state seems to be reached around $t = 50$ for $\gamma = +0.5$, after which time the wave height stagnates at $a_{\max} \simeq 0.2 < a$ and the wave shape remains overall preserved. Small fluctuations are discernible due to interaction of the pulse with the low-amplitude ambient radiation. The latter is produced during the early stages when the initial solitary wave enters the rotational field, and then it contaminates the entire domain via the periodic boundary conditions. Note that the two pulses at $t = 50$ and $t = 500$ look close together but the solution has actually traveled

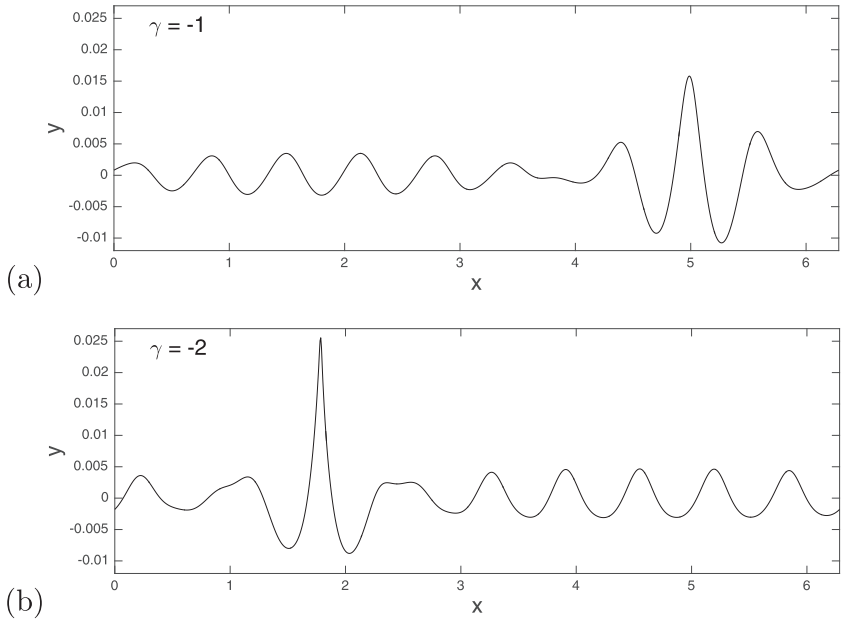

Fig. 4. Snapshots of η at (a) $t = 586$ ($\gamma = -1$) and (b) $t = 376$ ($\gamma = -2$) for an initially perturbed Stokes wave of amplitude $a = 0.005$ and wavenumber $\kappa = 10$ on deep water.

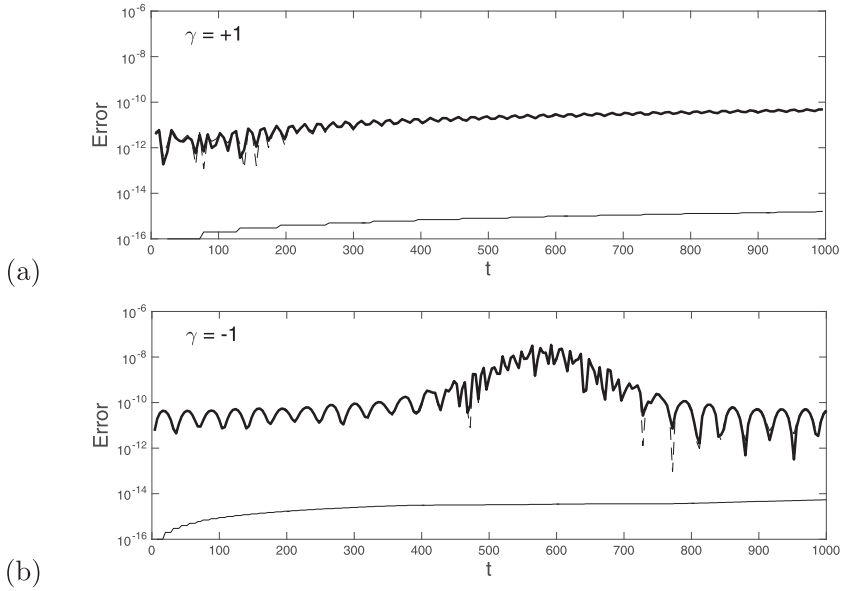

Fig. 5. Time evolution of errors on energy H (thick solid line), impulse I (dashed line) and volume V (thin solid line) for an initially perturbed Stokes wave on deep water in the presence of a linear shear current with vorticity (a) $\gamma = +1$ and (b) $\gamma = -1$.

several times through the computational domain during this time interval because of the periodic boundary conditions. On the other hand, for $\gamma = -0.5$, the counter-propagating current is so strong that the solitary wave quickly steepens and grows to reach a height $a_{\max} = 0.516$ at $t = 25$. This most likely leads to wave breaking and the computer code breaks down shortly afterward. Unlike the previous situation with a Stokes wave where intense focusing occurs sporadically after a succession of modulations and demodulations, the present case shows a solitary wave that is continually amplified as it travels against a strong opposing current.

Results are slightly different if $|\gamma|$ is smaller, as depicted in Fig. 7. For $\gamma = -0.3$, the counter-propagating current only causes the wave height to increase up to $a_{\max} \simeq 0.4 > a$ and, after $t \simeq 50$, a near-steadily progressing pulse emerges and coexists with smaller ambient radiation. This is similar to what happens in the case $\gamma = +0.5$ during the late stages (Fig. 6b and c), but here the emerging pulse is taller than the initial solitary wave. For $\gamma = +0.3$, the scenario is even closer to that for $\gamma = +0.5$ (both involving a co-propagating current), with the difference that the emerging wave height is much less than the initial one because of the weaker vorticity, and so these results are not shown here for convenience. As with Stokes waves, the extent to which a solitary wave is amplified (or reduced) is directly related to the vortical strength. Our direct time-dependent simulations also suggest that, if $|\gamma|$ is not too large, there exist large-amplitude rotational solitary waves that would travel steadily without change of speed and shape in the absence of disturbances. Moreover, they seem to be stable since they remain mostly unaffected by the surrounding radiation. These results support the theoretical predictions of [24,32] and [48] on the existence of solitary waves with vorticity,

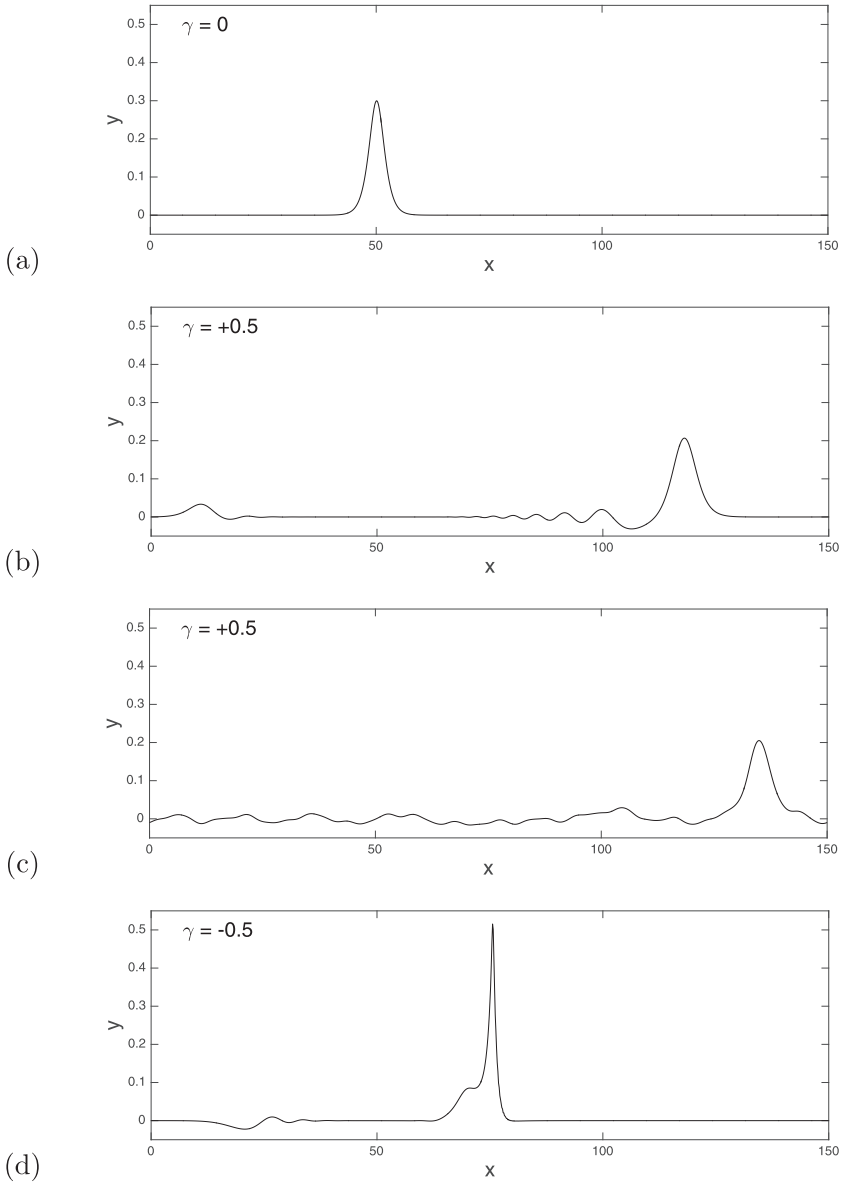

Fig. 6. Snapshots of η at (a) $t = 0$ ($\gamma = 0$), (b) $t = 50$ ($\gamma = +0.5$), (c) $t = 500$ ($\gamma = +0.5$) and (d) $t = 25$ ($\gamma = -0.5$) for an initial solitary wave of height $a = 0.3$ on shallow water.

as well as the recent computations of [36] based on the (weakly dispersive) Green–Naghdi equations.

To further quantify the effects of vorticity, we perform a direct comparison between an irrotational solitary wave computed by Tanaka's method and our rotational solution for a given amplitude. Two cases are presented in Fig. 8 for $a_{\max} = 0.2$ ($\gamma = +0.5$) and $a_{\max} = 0.4$ ($\gamma = -0.3$). On each graph, the two curves are superimposed in such a way that their central crests coincide. Snapshots of the rotational solution are chosen at a late time after relaxation to the equilibrium state. We observe that, if $\gamma < 0$ (resp. $\gamma > 0$), the rotational solitary wave tends to be thinner (resp. broader) than the irrotational one. Similar differences in wave shape were highlighted by [1] and [36] in the context of long-wave models. Although the fluctuations due to interaction with the ambient radiation are more apparent in the lower-amplitude solution ($a_{\max} = 0.2$), it is clear from Fig. 8 that a co-propagating current ($\gamma > 0$) has a broadening effect on the surface wave profile. Finally, the conservation of H, I and V is illustrated in Fig. 9 for $\gamma = \pm 0.3$. Time evolution of the relative error is plotted for each of these quantities. Again, we see that all three of them are very well conserved, with the errors on V being considerably lower (near machine precision) than those for H and I. The latter errors can certainly be improved by specifying finer discretizations in space and time, but they are found to be quite satisfactory for the present purposes.

5. Conclusions

We have proposed a direct numerical solver for the full time-dependent equations describing two-dimensional nonlinear water waves over arbitrary (uniform) depth with nonzero constant vorticity, based on the Hamiltonian formulation of [45] and [9]. As an extension of the numerical approach of [17], our solver reduces the original Laplace problem to a lower-dimensional computation involving surface variables alone. This is accomplished by introducing the DNO and associated HT which are expressed in terms of a convergent Taylor series expansion about the unperturbed geometry of the fluid domain. Each term in these Taylor series is determined recursively and computed efficiently by a pseudo-spectral method using the FFT. In particular, we have derived a new recur-

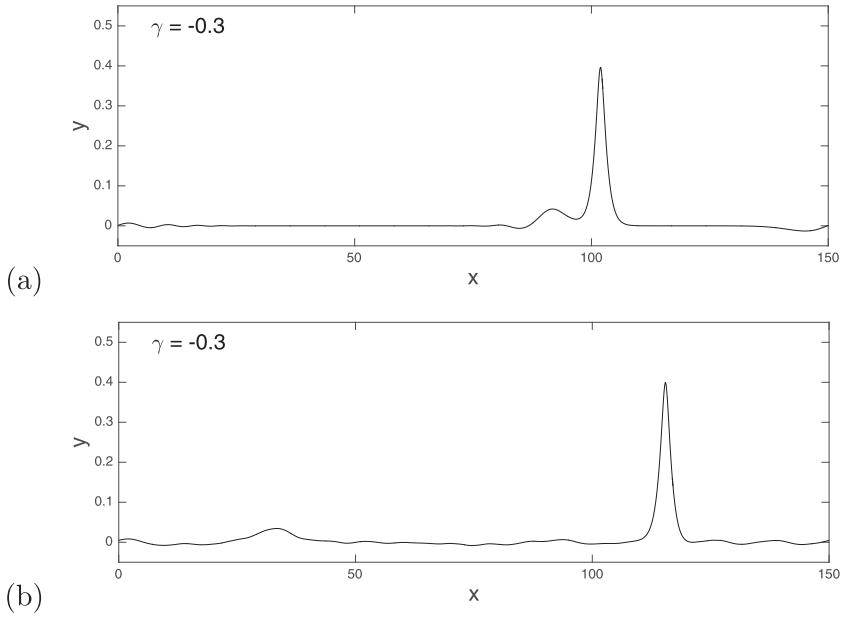

Fig. 7. Snapshots of η at (a) $t = 50$ and (b) $t = 500$ for an initial solitary wave of height $a = 0.3$ on shallow water in the presence of a linear shear current with vorticity $\gamma = -0.3$.

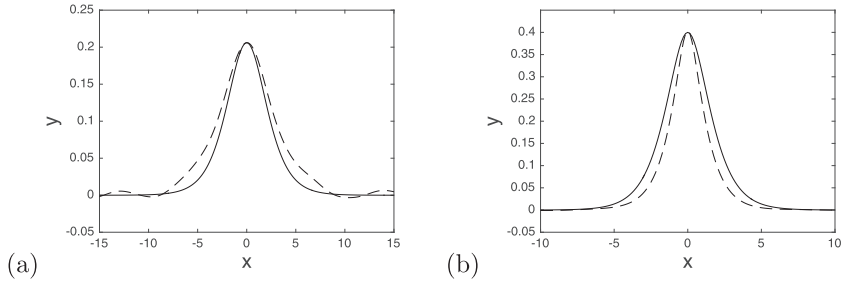

Fig. 8. Comparison between an irrotational solitary wave computed by Tanaka's method (solid line) and our rotational solution (dashed line) for (a) $a_{\max} = 0.2$ ($\gamma = +0.5$) at $t = 310$ and (b) $a_{\max} = 0.4$ ($\gamma = -0.3$) at $t = 465$. On each graph, the two curves are re-centered at $x = 0$.

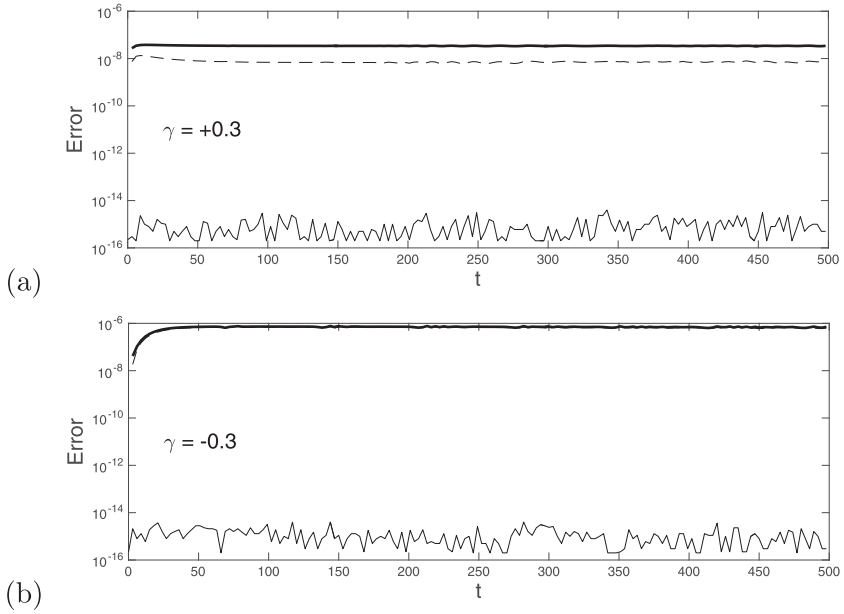

Fig. 9. Time evolution of errors on energy H (thick solid line), impulse I (dashed line) and volume V (thin solid line) for an initial solitary wave on shallow water in the presence of a linear shear current with vorticity (a) $\gamma = +0.3$ and (b) $\gamma = -0.3$.

sion formula to evaluate the HT in its series form, where each term is given as a sum of concatenations of Fourier multipliers with powers of the surface elevation.

We have performed extensive tests to assess the convergence of this Taylor series for the HT, with respect to various physical and numerical parameters. Our tests confirm the exponential convergence with the order of truncation M but, as reported in prior work on the DNO, there is an optimal value of M above which the convergence quickly deteriorates. This numerical issue is attributed to ill-conditioning of the series expansion in the sense that round-off errors are amplified through the recursive process for determining the Taylor terms. The finer the spatial resolution or the larger the wave amplitude/steepness, the smaller this optimal value.

By transforming the system of partial differential equations into a system of ordinary differential equations for the Fourier coefficients, the pseudo-spectral method for space discretization also allows stiff linear terms to be solved exactly in time via the integrating factor technique. The remaining terms are solved numerically in time by a fourth-order Runge–Kutta method without the need for using an excessively small time step. The overall scheme is shown to have excellent conservative properties with such quantities as energy, impulse and volume being very well conserved over long times.

We have applied our numerical model to simulating nonlinear solutions in two distinct limiting regimes: Stokes waves on deep water and solitary waves on shallow water. A co-propagating background current ($\gamma > 0$) is found to have a stabilizing, and even attenuating, effect on surface wave dynamics. If γ is large enough, the BFI of Stokes waves may be completely inhibited while solitary waves are significantly reduced in amplitude. A counter-propagating current ($\gamma < 0$) on the other hand tends to amplify surface waves. In particular, it promotes and enhances the BFI of Stokes waves (by making it happen sooner with a larger wave growth). If the opposing current is too strong, wave breaking eventually occurs and the computer code breaks down. Our numerical results also suggest the existence of stable rotational solitary waves in the fully nonlinear and fully dispersive setting, if $|\gamma|$ is not too large.

Recently, there has been growing interest in the water wave problem with more general types of vorticity such as compactly supported vorticity [18,41]. It would be of interest in the future to explore the possibility of extending the present numerical model to such cases. The Transformed Field Expansion method of [38] would also be an option to consider in order to improve the numerical convergence of the DNO and HT.

Acknowledgement

The author is partially supported by the NSF under grant No. DMS-1615480 and the Simons Foundation under grant No. 246170.

References

[1] Ali A, Kalisch H. Reconstruction of the pressure in long-wave models with constant vorticity. Eur J Mech B Fluids 2013;37:187–94.
[2] Ashton ACL, Fokas AS. A non-local formulation of rotational water waves. J Fluid Mech 2011;689:129–48.
[3] Benjamin TB, Feir JE. The disintegration of wave trains on deep water. Part 1. Theory. J Fluid Mech 1967;27:417–30.
[4] Canuto C, Hussaini MY, Quarteroni A, Zang TA. Spectral methods in fluid dynamics. Springer–Verlag, Berlin; 1987.
[5] Castro A, Lannes D. Well-posedness and shallow-water stability for a new Hamiltonian formulation of the water waves equations with vorticity. Indiana Univ Math J 2015;64:1169–270.
[6] Choi W. Nonlinear surface waves interacting with a linear shear current. Math Comput Simul 2009;80:29–36.
[7] Coifman R, Meyer Y. Nonlinear harmonic analysis and analytic dependence. Proc Symp Pure Math 1985;43:71–8.
[8] Compelli A. Hamiltonian formulation of 2 bounded immiscible media with constant non-zero vorticities and a common interface. Wave Motion 2015;54:115–24.
[9] Constantin A, Ivanov RI, Prodanov EM. Nearly-Hamiltonian structure for water waves with constant vorticity. J Math Fluid Mech 2008;10:224–37.
[10] Constantin A, Strauss W. Exact steady periodic water waves with vorticity. Commun Pure Appl Math 2004;57:481–527.
[11] Craig W, Guyenne P, Hammack J, Henderson D, Sulem C. Solitary water wave interactions. Phys Fluids 2006;18:057106.
[12] Craig W, Guyenne P, Kalisch H. Hamiltonian long wave expansions for free surfaces and interfaces. Commun Pure Appl Math 2005;58:1587–641.
[13] Craig W, Guyenne P, Sulem C. Water waves over a random bottom. J Fluid Mech 2009;640:79–107.
[14] Craig W, Guyenne P, Sulem C. A Hamiltonian approach to nonlinear modulation of surface water waves. Wave Motion 2010;47:552–63.
[15] Craig W, Guyenne P, Sulem C. The surface signature of internal waves. J Fluid Mech 2012;710:277–303.
[16] Craig W, Nicholls DP. Traveling gravity water waves in two and three dimensions. Eur J Mech B Fluids 2002;21:615–41.
[17] Craig W, Sulem C. Numerical simulation of gravity waves. J Comput Phys 1993;108:73–83.
[18] Curtis CW, Kalisch H. Vortex dynamics in nonlinear free surface flows. Phys Fluids 2017;29:032101.
[19] Curtis CW, Oliveras KL, Morrison T. Shallow waves in density stratified shear currents. Eur J Mech B Fluids 2017;61:100–11.
[20] Dalrymple RA. A finite amplitude wave on a linear shear current. J Geophys Res 1974;79:4498–504.
[21] Dommermuth DG, Yue DKP. A high-order spectral method for the study of nonlinear gravity waves. J Fluid Mech 1987;184:267–88.
[22] Fenton JD. The numerical solution of steady water wave problems. Comput Geosci 1988;14:357–68.
[23] Francius M, Kharif C, Viroulet S. Nonlinear simulations of surface waves in finite depth on a linear shear current. In: Proc. 7th int. conf. coastal dynamics; 2013. p. 649–60.
[24] Groves MD, Wahlén E. Small-amplitude Stokes and solitary gravity water waves with an arbitrary distribution of vorticity. Physica D 2008;237:1530–8.
[25] Guyenne P. Envelope equations for three-dimensional gravity and flexural-gravity waves based on a Hamiltonian approach. Fields Inst Commun 2015;75:135–61.
[26] Guyenne P, Grilli ST. Numerical study of three-dimensional overturning waves in shallow water. J Fluid Mech 2006;547:361–88.
[27] Guyenne P, Lannes D, Saut J-C. Well-posedness of the Cauchy problem for models of large amplitude internal waves. Nonlinearity 2010;23:237–75.
[28] Guyenne P, Nicholls DP. A high-order spectral method for nonlinear water waves over moving bottom topography. SIAM J Sci Comput 2007;30:81–101.
[29] Guyenne P, Părău EI. Computations of fully nonlinear hydroelastic solitary waves on deep water. J Fluid Mech 2012;713:307–29.
[30] Guyenne P, Părău EI. Numerical study of solitary wave attenuation in a fragmented ice sheet. Phys Rev Fluids 2017;2:034002.
[31] Hou TY, Lowengrub JS, Shelley MJ. Removing the stiffness from interfacial flows with surface tension. J Comput Phys 1994;114:312–38.
[32] Hur VM. Exact solitary water waves with vorticity. Arch Ration Mech Anal 2008;188:213–44.
[33] Kharif C, Pelinovsky E. Physical mechanisms of the rogue wave phenomenon. Eur J Mech B Fluids 2003;22:603–34.
[34] King FW. Hilbert transforms. Cambridge University Press, Cambridge; 2010.
[35] Ko J, Strauss W. Large-amplitude steady rotational water waves. Eur J Mech B Fluids 2008;27:96–109.
[36] Lannes D, Marche F. Nonlinear wave-current interactions in shallow water. Stud Appl Math 2016;136:382–423.
[37] Moreira RM, Peregrine DH. Nonlinear interactions between deep-water waves and currents. J Fluid Mech 2012;691:1–25.
[38] Nicholls DP, Reitich F. Stability of high-order perturbative methods for the computation of Dirichlet–Neumann operators. J Comput Phys 2001;170:276–98.
[39] Nicholls DP, Reitich F. Analytic continuation of Dirichlet–Neumann operators. Numer Math 2003;94:107–46.
[40] Phillips OM. The dynamics of the upper ocean. Cambridge University Press, Cambridge; 1977.
[41] Shatah J, Walsh S, Zeng C. Travelling water waves with compactly supported vorticity. Nonlinearity 2013;26:1529–64.
[42] Swan C, Cummins IP, James RL. An experimental study of two-dimensional surface water waves propagating on depth-varying currents. J Fluid Mech 2001;428:273–304.
[43] Tanaka M. The stability of solitary waves. Phys Fluids 1986;29:650–5.
[44] Vanden-Broeck J-M. Periodic waves with constant vorticity in water of infinite depth. IMA J Appl Math 1996;56:207–17.
[45] Wahlén E. A hamiltonian formulation of water waves with constant vorticity. Lett Math Phys 2007;79:303–15.
[46] Wahlén E. Hamiltonian long-wave approximations of water waves with constant vorticity. Phys Lett A 2008;372:2597–602.
[47] West BJ, Brueckner KA, Janda RS, Milder DM, Milton RL. A new numerical method for surface hydrodynamics. J Geophys Res 1987;92:11803–24.
[48] Wheeler MH. Large-amplitude solitary water waves with vorticity. SIAM J Math Anal 2013;45:2937–94.
[49] Xu L, Guyenne P. Numerical simulation of three-dimensional nonlinear water waves. J Comput Phys 2009;228:8446–66.
[50] Zakharov VE. Stability of periodic waves of finite amplitude on the surface of a deep fluid. J Appl Mech Tech Phys 1968;9:190–4.